

An extended lumped-element model and parameter estimation technique to predict loudspeaker responses with possible surround-dip effects

Jason D. Sagers^{a)}

*Acoustics Research Group, Department of Mechanical Engineering, 435 Crabtree Building,
Brigham Young University, Provo, Utah 84602*

Timothy W. Leishman^{b)}

*Acoustics Research Group, Department of Physics and Astronomy, N283 Eyring Science Center,
Brigham Young University, Provo, Utah 84602*

Jonathan D. Blotter

*Acoustics Research Group, Department of Mechanical Engineering, 435 Crabtree Building,
Brigham Young University, Provo, Utah 84602*

(Received 5 January 2013; revised 14 August 2013; accepted 15 August 2013)

Lumped-element models have long been used to estimate the basic vibration and radiation characteristics of moving-coil loudspeakers. The classical low-frequency model combines and simplifies several important driver elements, predicting only a single mechanical resonance wherein the diaphragm (e.g., cone and dust cap) and the inner portion of the surround move together as an effective piston. Even if the diaphragm maintains piston-like motion with increasing frequency, the flexible surround eventually vibrates out of phase, producing another resonance whereby a noticeable “surround dip” may occur in the radiated pressure spectrum. The classical model is unable to predict this behavior. This paper explores an extended lumped-element model that better characterizes the distinct diaphragm, surround, spider, and other properties of a loudspeaker in a plane rigid baffle. It extends effective modeling to mid frequencies and readily predicts a surround dip in the radiated response. The paper also introduces a method to estimate model parameters using a scanning laser Doppler vibrometer, a surround resonance indicator function, and a constrained optimization routine. The approach is validated by its ability to better predict on-axis pressure responses of several baffled loudspeakers in an anechoic environment.

© 2013 Acoustical Society of America. [<http://dx.doi.org/10.1121/1.4820886>]

PACS number(s): 43.38.Dv, 43.38.Ja, 43.40.At, 43.20.Ye [DDE]

Pages: 3580–3593

I. INTRODUCTION

The classical lumped-element model of a moving-coil loudspeaker is based partly on the assumption that the radiating surfaces behave as a flat vibrating piston with an effective area equal to the projected area of the diaphragm (e.g., cone and dust cap) plus an inner portion of the surround.^{1–4} The moving mass of the complete diaphragm assembly and the compound compliance and resistance of the suspension characterize its mechanical behavior, including its principal resonance.¹ While this single-degree-of-freedom model may be adequate for very low-frequency radiation predictions, it is typically inadequate for higher frequencies. Even if a well-designed diaphragm continues to vibrate in piston-like fashion, its flexible surround begins to vibrate out of phase as frequency increases to a second resonant state. Because the surround involves appreciable surface area, its contribution to radiation should not be overlooked.

A “surround dip” has often been observed in loudspeaker frequency response measurements,^{5–7} but to the knowledge of the authors, its fundamental bases have not been efficiently represented in an electro-mechano-acoustical circuit for loudspeaker design and performance predictions. This paper investigates a straightforward extension of the classical model that includes a central piston representing the diaphragm and a concentric annular piston representing the surround. The two are coupled with mechanical compliance and resistance, and are connected independently to the driver frame (basket) with distinct mechanical compliances and resistances.

The authors have previously investigated active sound transmission control modules with similar properties,^{8,9} but only in the context of one-dimensional sound transmission for normally incident and transmitted plane waves. True employed destructive experimental techniques and basic calculations to isolate surround and spider compliances from their compound compliance,¹⁰ but he did not incorporate them into a model or consider associated resistances and effective surround masses. Beranek’s divided-diaphragm representation was also relevant,¹ but its focus was not on diaphragm-surround interactions and it lacked several critical modeling elements.

To successfully represent the radiating loudspeaker, the extended model must incorporate appropriate self and

^{a)}Current address: Applied Research Laboratories, The University of Texas at Austin, P.O. Box 8029, Austin, TX 78713-8029.

^{b)}Author to whom correspondence should be addressed. Electronic mail: tim_leishman@byu.edu

mutual radiation impedances for the two pistons, and its parameters must be measurable to enable subsequent modeling of complete systems.^{11,12} This paper addresses these and other deficiencies by exploring the model, introducing a parameter estimation technique, and validating the ability of the tools to estimate on-axis pressure responses of baffled loudspeakers¹³ in an anechoic environment.

The proposed two-degree-of-freedom representation does not characterize higher-order interactions, modal behaviors, or “breakup” of diaphragms and surrounds at high frequencies,^{1,14–16} nor does it fully characterize rim resonances.^{17,18} However, with appropriate parameter values, it does provide a tractable means of improving radiated response predictions through mid frequencies, while anticipating basic surround dip effects. It does so through the use of effective diaphragm and surround velocities and other electro-mechano-acoustical driver properties.

More extensive computational models, such as finite-element and boundary-element models, could yield more detailed information. However, they typically fail to address a driver as an electro-mechano-acoustical whole and efficiently coalesce with simpler multi-domain loudspeaker modeling tools (e.g., analogous circuits) in the complete loudspeaker design process. Key attributes of a successful loudspeaker driver model include its ability to efficiently synthesize complete loudspeaker systems (including enclosures, crossovers, etc.) and to predict acoustic radiation to a listener or receiver. While lumped-element analogous-circuit models have limited capabilities, they have long been used to fulfill these aims and continue to serve as valuable tools in multiple-parameter loudspeaker characterizations.

Section II reviews several features of the classical model that are pertinent to this investigation. Sections III–V explore the extended model, a method for estimating its parameters using a scanning laser Doppler vibrometer (SLDV), and an experimental validation of its ability to predict on-axis pressure responses.

II. CLASSICAL MODEL

The classical lumped-element model^{1,19} of a moving-coil loudspeaker driver is illustrated in Fig. 1 (see the List of Symbols for clarifications). It is widely used by acousticians and audio engineers because of its familiarity, simplicity, and well-established parameter estimation techniques.^{20,21} A resilient surround is not explicitly shown connecting the diaphragm to the frame because the model does not duly account for its presence. Instead, its effective mechanical compliance and resistance are combined with those of the spider to produce a compound compliance C_{MS} and compound resistance R_{MS} . Its mass and surface area are also combined with those of the remaining diaphragm assembly components to form an effective piston-like moving mass M_{MD} and radiating area S_D . Sections II A–II C clarify the role of the piston as a diaphragm assembly representation, then consider the effective radiating area and analogous circuit of the model. Many concepts in these sections also apply to the extended model discussed in Sec. III.

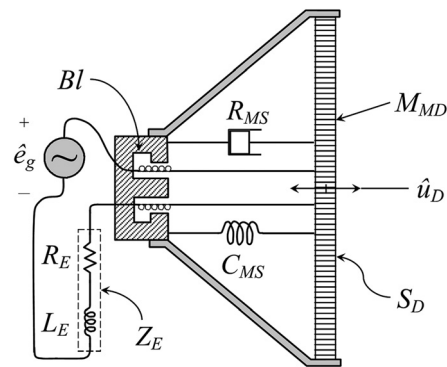


FIG. 1. A diagram showing the key components of the classical moving-coil loudspeaker driver model.

A. Planar piston representation

Most woofers, mid-bass drivers, and full-range drivers incorporate conical, concave, or other nonplanar radiating surfaces that vibrate with nearly axial, rigid-body motion at sufficiently low frequencies (i.e., below cone breakup). A flat, piston-like representation of these surfaces can be justified under certain conditions. Their radiated pressures may be estimated using the complete Kirchhoff-Helmholtz integral equation^{22,23} or the related boundary element method. However, because these approaches were impractical during the development of the classical model, a reduced single-integral formula was sought to predict results for vibrating diaphragm assemblies in an infinite plane rigid baffle. The difficulty in defining appropriate Green’s functions and evaluating the integral led to the use of the half-space Green’s function $G_{hs}(\mathbf{r}|\mathbf{r}_S) = 2 \exp(-jkR)/R$ as a tractable approximation.^{3,24–26} The resulting formulation corresponds to the (first) Rayleigh integral,^{22,23} commonly used for planar source distributions:

$$\hat{p}(\mathbf{r}) \approx \frac{j\omega\rho_0}{2\pi} \iint_S \hat{u}_{Sn}(\mathbf{r}_S) \frac{e^{-jkR}}{R} dS. \quad (1)$$

For a nonplanar diaphragm assembly, the complex normal surface velocity amplitude $\hat{u}_{Sn}(\mathbf{r}_S)$ is nonzero only on its surface and is not necessarily normal to the baffle plane. In addition, $R = |\mathbf{r} - \mathbf{r}_S|$ represents the distance from the point \mathbf{r}_S on the assembly (not necessarily on the baffle plane) to the field point \mathbf{r} . If the assembly is circular and vibrates with axial rigid-body motion, the field is axisymmetric and may be readily evaluated using simple numerical techniques.

One useful idealization of a common loudspeaker diaphragm is a baffled right-circular cone with uniform axial surface velocity $\hat{u}_{Sa} = \hat{u}_{Sn}/\sin\alpha$, where α is the cone semi-apex angle. The position vectors \mathbf{r} and \mathbf{r}_S are often assumed to originate from the cone apex at $z < 0$ rather than the baffle plane at $z = 0$. If \mathbf{r} falls in the geometric far field such that $r \gg r_s$, the pressure relationship becomes

$$\hat{p}(r, \theta) \approx j\omega\rho_0 \hat{u}_{Sa} \sin^2\alpha \frac{e^{-jkr}}{r} \times \int_0^{h_s} e^{jkr_S \cos z \cos \theta} J_0(kr_S \sin \alpha \sin \theta) r_S dr_S, \quad (2)$$

where h_s is the cone slant height, θ is the angle between \mathbf{r} and the cone axis, $\theta \leq \alpha$, and J_0 is the zeroth-order Bessel function of the first kind (compare Refs. 24–26). For on-axis field points, integration yields the complex pressure amplitude

$$\hat{p}(r, 0) \approx j\omega\rho_0\hat{u}_{sa}a_b^2 \frac{e^{-jkr}}{r} \left[\frac{e^{jkh}(1-jkh) - 1}{(kh)^2} \right], \quad (3)$$

where $a_b = h_s \sin \alpha$ is the cone base radius and $h = h_s \cos \alpha$ is the cone height. If $kh \ll 1$,

$$\hat{p}(r, 0) \rightarrow \frac{j\omega\rho_0\hat{u}_{sa}a_b^2}{2} \frac{e^{-jkr}}{r}, \quad (4)$$

meaning the pressure converges to the on-axis pressure produced by a baffled circular piston of radius a_b (for $r \gg \pi a_b^2/2\lambda$).²⁷ However, if $kh \gg 1$,

$$\hat{p}(r, 0) \rightarrow \rho_0 c \hat{u}_{sa} a_b^2 \frac{e^{-jkr}}{r} \frac{e^{jkh}}{h}, \quad (5)$$

which clearly differs. A transition between the extremes occurs near $kh \approx 2$ or $ka_b \approx 2 \tan \alpha$.²⁶

An effective planar piston may thus be considered to generate the far-field on-axis pressure produced by a conical diaphragm if (1) $f \leq c \tan \alpha / \pi a_b$, (2) the normal complex piston velocity amplitude equals the uniform axial cone velocity amplitude \hat{u}_{sa} , and (3) the piston area equals the cone base (projected) area πa_b^2 . Because similar findings have been reported for other diaphragm geometries,³ the planar piston may be considered a reasonable approximation for a typical diaphragm assembly at sufficiently low frequencies. However, as indicated earlier, it fails to account for nonuniform vibrations in the diaphragm assembly without the use of additional approximations.

B. Effective radiating area

As suggested in Fig. 2, the effective radiating area $S_D = \pi a_D^2$ of a diaphragm assembly involving a cone, dust cap, and surround is often estimated using basic geometrical arguments. Some have treated the central diaphragm region as a uniformly vibrating surface with axial displacement $z_s(t)$ and the surround as a nonuniformly vibrating surface

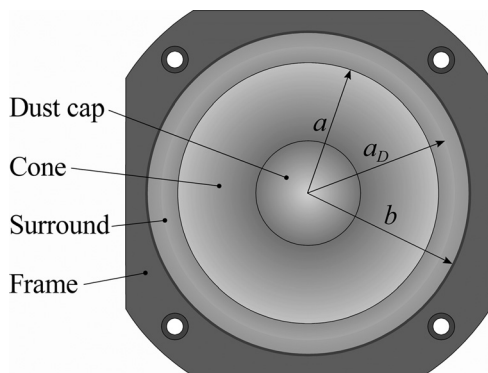


FIG. 2. A diagram showing the radiating diaphragm assembly components and radii used in the text.

with displacement tapering linearly from $z_s(t)$ at its inner perimeter to zero at its outer perimeter.^{3,4,21} The volume $V(t)$ displaced by a circular diaphragm assembly thus corresponds to that of a right circular conical frustum with effective area

$$S_D = \frac{V(t)}{z_s(t)} = \frac{\pi}{3}(a^2 + ab + b^2) \quad (6)$$

and effective radius

$$a_D = \sqrt{\frac{S_D}{\pi}} \approx \sqrt{\frac{a^2 + ab + b^2}{3}} \approx a \sqrt{1 + \frac{b-a}{a} + \frac{1}{3} \left(\frac{b-a}{a} \right)^2}. \quad (7)$$

When $(b-a)/a \ll 1$, the latter converges to the common approximation $a_D \approx (a+b)/2$, the projected radius from the center of the diaphragm to the midpoint of the surround.

Because uniform diaphragm displacement and linear surround taper cannot be guaranteed, S_D should be characterized more carefully in terms of measurable physical effects. Beranek recommended its derivation from the incremental static pressure within a sealed rigid enclosure after the diaphragm of a coupled loudspeaker had been displaced a known distance (at an unspecified reference position).^{1,21} More suitable dynamic approaches consider the area to be that of a piston producing the same frequency-dependent acoustic effect(s) as the diaphragm assembly while vibrating with a normal complex velocity amplitude \hat{u}_D . The targeted effect(s) and definitions of \hat{u}_D have varied in the literature.

Frankort suggested that the effective piston area should produce similar on-axis far-field pressure and sound power responses at low-to-mid frequencies when \hat{u}_D is idealized as the axial velocity \hat{u}_{sa} of a rigid-body cone.²⁶ Both he and Brown²⁴ found that the off-axis pressure response of the piston differs considerably from that of the ideal cone at higher frequencies because of dissimilar frequency-dependent directivities. Anthony and Elliott indicated that the effective piston area should produce the same volume velocity when \hat{u}_D is defined as the low-frequency axial velocity of the diaphragm assembly at an arbitrary surface position.²⁸ Jönsson recommended that the area be determined from the classical relationship between V_{AS} and C_{MS} , where V_{AS} follows from the frequency response function (FRF) (i.e., transfer function) between the voice-coil current and the axial surface velocity (at an indefinite position) while the driver is mounted on a sealed enclosure.²⁹ D'Appolito reasoned that it should follow directly from added-mass and added-compliance (closed-box) perturbation measurements, while satisfying classical loudspeaker equations independent of \hat{u}_D .²⁰ Moreno *et al.* suggested that the area should produce the same on-axis near-field pressure magnitude at $z=0$ when \hat{u}_D is the low-frequency axial velocity of the diaphragm at an arbitrary position.³ Klippel and Schlechter stated that it should produce the same on-axis far-field pressure and volume velocity when \hat{u}_D is the axial, circumferentially averaged voice-coil velocity over a broad frequency range. They also considered its production of equivalent acoustic pressures within small, coupled cavities.⁴

While the precise matching of every possible acoustic outcome by an effective piston is infeasible, more could be done to optimize the matching of any one effect or a multiplicity of effects. Sections II B 1 and II B 2 clarify the matching of volume velocity by a hypothetical piston and the significance of the related acoustic radiation impedance.

1. Volume velocity

Volume velocity is the rate of sound-induced flow of an acoustic medium through an actual or hypothetical surface S , expressed in terms of particle velocity $\hat{\mathbf{u}}(\mathbf{r}_S)$ as²²

$$\hat{U} = \int \int_S \hat{\mathbf{u}}(\mathbf{r}_S) \cdot \mathbf{n}_S dS, \quad (8)$$

where \mathbf{n}_S is the unit vector normal to the surface. It may be approximated through the summed volume velocities of much smaller discrete elements ΔS_i , each of which has a presumably uniform particle velocity $\hat{\mathbf{u}}_i$, as

$$\hat{U} \approx \sum_{i=1}^I \hat{\mathbf{u}}_i \cdot \mathbf{n}_{S,i} \Delta S_i = \sum_{i=1}^I \hat{u}_i \cos \theta_i \Delta S_i = \sum_{i=1}^I \hat{u}_{n,i} \Delta S_i, \quad (9)$$

where θ_i is the angle between $\hat{\mathbf{u}}_i$ and the element normal $\mathbf{n}_{S,i}$. If a hypothetical planar surface lies close and parallel to a driver face (i.e., perpendicular to its axis) the normal (axial) particle velocity components $\hat{u}_{n,i}$ should be evaluated at several points on the surface, then area weighted and summed to represent the volume velocity through it. However, axial surface velocities $\hat{u}_{Sa,i}$ are typically measured at several positions on the underlying diaphragm assembly (e.g., using an axially oriented SLDV), then mapped to the associated, projected elements on the hypothetical surface as though they were particle velocity components themselves.^{4,28}

In many cases, the preferred discrete-point measurement of the diaphragm assembly is the velocity FRF between the signal-generator voltage \hat{e}_g driving the loudspeaker and $\hat{u}_{Sa,i}$ (Ref. 28):

$$H_i(f) = \frac{\hat{u}_{Sa,i}}{\hat{e}_g}. \quad (10)$$

A total volume-velocity FRF then follows as

$$H(f) = \frac{\hat{U}}{\hat{e}_g} \approx \sum_{i=1}^I \frac{\hat{u}_{Sa,i}}{\hat{e}_g} \Delta S_i = \sum_{i=1}^I H_i(f) \Delta S_i. \quad (11)$$

The axial velocity (or velocity FRF) of any element may be used to estimate the total volume velocity (or volume velocity FRF), but only if the effective radiating area of the assembly has been properly defined. For the j th reference element, Eqs. (9)–(11) yield the required relationships

$$S_{D,j}(f) = \frac{\hat{U}}{\hat{u}_{Sa,j}} \approx \frac{1}{\hat{u}_{Sa,j}} \sum_{i=1}^I \hat{u}_{Sa,i} \Delta S_i \quad (12)$$

and

$$S_{D,j}(f) = \frac{H(f)}{H_j(f)} \approx \frac{1}{H_j(f)} \sum_{i=1}^I H_i(f) \Delta S_i, \quad (13)$$

both of which are frequency dependent (as one might expect for a dynamic system), reference-position dependent, and complex. Anthony and Elliott found that some reference positions reduce the frequency dependence and the imaginary part.²⁸ Klippel and Schlechter observed that the calculated areas tend to have nearly constant, real values for in-phase vibrations at low frequencies.⁴

The choice of the j th element in these calculations is completely arbitrary; it does not necessarily coincide with the circumference delineated by the coil former attachment to the diaphragm. However, because electromechanical driver coupling depends explicitly upon axial voice-coil velocity, it stands to reason that the element should fall on or near the circumference. If the axial surface velocity is not uniform around the circumference, it may be averaged as suggested by Kippel and Schlechter.⁴ If it cannot be scanned directly because of an intervening dust cap or other structural features, an effort should be made to measure the voice-coil velocity as accurately as possible to support the model.

2. Acoustic radiation impedance

The effective radiating area couples the mechanical impedance (or mobility) representation of the driver to its acoustic impedance representation. Acoustic impedance is the ratio of weighted spatially averaged pressure to volume velocity across a hypothetical or vibrating surface.^{22,30} The acoustic radiation impedance Z_{AR} seen by the diaphragm assembly is then

$$\begin{aligned} Z_{AR} &= \frac{\langle \hat{p}(\mathbf{r}_S) \rangle_{S,w}}{\hat{U}} = \frac{\langle \hat{p}(\mathbf{r}_S) \rangle_{S,w}}{S \langle \hat{u}_{Sn}(\mathbf{r}_S) \rangle_S} \\ &= \frac{1}{S \langle \hat{u}_{Sn}^*(\mathbf{r}_S) \rangle_S} \int \int_S \hat{p}(\mathbf{r}_S) \hat{\mathbf{u}}_S^*(\mathbf{r}_S) \cdot \mathbf{n}_S dS \\ &= \frac{1}{\int \int_S \hat{\mathbf{u}}_S(\mathbf{r}_S) \cdot \mathbf{n}_S dS} \int \int_S \hat{p}(\mathbf{r}_S) \hat{\mathbf{u}}_S^*(\mathbf{r}_S) \cdot \mathbf{n}_S dS = \frac{Z_{MR}}{S^2}, \end{aligned} \quad (14)$$

where S is its total surface area and Z_{MR} is the associated mechanical radiation impedance. The half-space time-averaged power and on-axis far-field pressure magnitude then follow as

$$\langle W \rangle_t = \frac{1}{2} |\hat{U}|^2 \text{Re}\{Z_{AR}\} = \frac{1}{2} |\langle \hat{u}_{Sn}(\mathbf{r}_S) \rangle_S|^2 \text{Re}\{Z_{MR}\} \quad (15)$$

and

$$|\hat{p}(r)| = \sqrt{\frac{|\langle \hat{u}_{Sn}(\mathbf{r}_S) \rangle_S|^2 \text{Re}\{Z_{MR}\} Q_p \rho_0 c}{4\pi r^2}}, \quad (16)$$

respectively, where Q_p is the principal-axis directivity factor.²¹ Equations (8)–(16) demonstrate the importance of integrated and spatially averaged pressure and particle velocity over the surface.

C. Analogous circuit

A multiple-domain analogous circuit representing the time-harmonic behavior of the classical model may be represented as shown in Fig. 3. Two effective-area gyrators

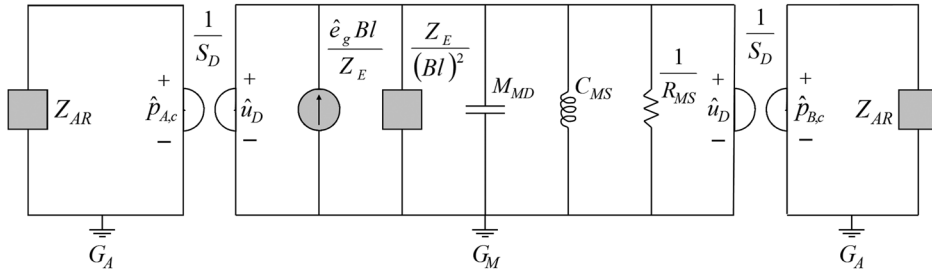


FIG. 3. A multiple-domain analogous circuit representing the classical model shown in Fig. 1. The complex diaphragm velocity amplitude is uniform and the complex acoustic pressure amplitudes are spatially averaged.

represent the coupling between the mechanical mobility and acoustic impedance domains. While the effective piston velocity amplitude \hat{u}_D is considered to be uniform, the complex acoustic pressure amplitudes $\hat{p}_{A,c}$ and $\hat{p}_{B,c}$ should technically be spatially averaged values. For an ideal loudspeaker mounted in an infinite plane rigid baffle, the acoustic radiation impedance Z_{AR} seen by the front of the diaphragm equals that seen by the back.

The electrical elements in the circuit have already been transformed into the mechanical mobility domain as an ideal flow source in parallel with a mobility element, the latter being proportional to the blocked electric impedance Z_E . For further simplification, all elements could be pulled through the gyrators and transformers to a single physical domain.²¹ Equations derived from the circuit enable the extraction of model parameters and the prediction of basic loudspeaker response characteristics.

III. EXTENDED MODEL

The extended model depicted in Fig. 4 contains several additional elements. The effective mass M_{M1} of the diaphragm is modeled separately from the effective mass M_{M2} of the surround. The compliance C_{M1} and resistance R_{M1} of the spider are also modeled separately from those of the surround. The compliance C_{M2} and resistance R_{M2} connecting the outer perimeter of the surround to the frame are modeled distinctly from the mutual compliance C_{M12} and resistance R_{M12} connecting the inner perimeter of the surround to the outer perimeter of the diaphragm. While not immediately apparent from the figure, these values are distributed uniformly around the stated perimeters. The model has two radiating surfaces: the circular piston-like diaphragm (with effective radiating area

S_1 and uniform normal velocity amplitude \hat{u}_1) and the annular piston-like surround (with effective radiating area S_2 and uniform normal velocity amplitude \hat{u}_2).

The multiple-domain analogous circuit representing the model is shown in Fig. 5. Four gyrators represent the coupling between the mechanical mobility and acoustic impedance domains. The self-acoustic radiation impedances Z_{A11} and Z_{A22} , and the mutual acoustic radiation impedance Z_{A12} of the pistons are included in the latter. They are assumed to be equal on the front and back sides for the ideal infinite-baffle case. As with the circuit in Fig. 3, the electrical elements have already been pulled into the mechanical mobility domain. Equations may again be derived from the circuit to aid in the extraction of model parameters and the prediction of vibro-acoustic responses.

As suggested earlier, the extended model is intended to improve predictive capabilities by eliminating unnecessary combinations of suspension and radiating surface elements. It better represents the distinct vibration and radiation characteristics of the diaphragm and surround, while predicting two system resonances instead of one. Nevertheless, it still assumes the vibrations are uniform and translational.

A. Key equations

The complex amplitudes \hat{u}_1 and \hat{u}_2 are key values of the extended model, represented as potential drops in the mechanical mobility portion of the circuit. Careful use of nodal analysis techniques and gyrator equations leads to solutions for these values and their associated velocity FRFs:

$$\frac{\hat{u}_1}{\hat{e}_g} = \frac{Bl}{Z_E} \left(\frac{Z_{MC}}{Z_{MA}Z_{MC} - Z_{MB}^2} \right), \quad (17)$$

$$\frac{\hat{u}_2}{\hat{e}_g} = \frac{Bl}{Z_E} \left(\frac{Z_{MB}}{Z_{MA}Z_{MC} - Z_{MB}^2} \right), \quad (18)$$

where

$$Z_{MA} = 2Z_{A11}S_1^2 + Z_{M1} + Z_{M12}, \quad (19)$$

$$Z_{MB} = Z_{M12} - 2Z_{A12}S_1S_2, \quad (20)$$

$$Z_{MC} = 2Z_{A22}S_2^2 + Z_{M2} + Z_{M12}, \quad (21)$$

and

$$Z_{M1} = \frac{(Bl)^2}{Z_E} + R_{M1} + \frac{1}{j\omega C_{M1}} + j\omega M_{M1}, \quad (22)$$

$$Z_{M2} = R_{M2} + \frac{1}{j\omega C_{M2}} + j\omega M_{M2}, \quad (23)$$

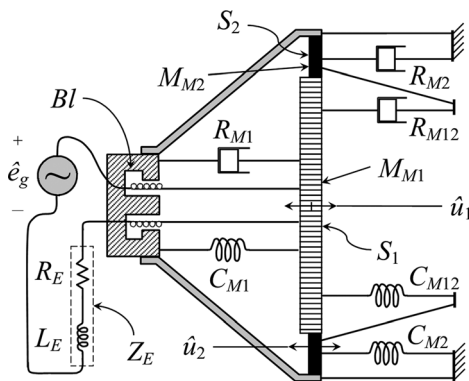


FIG. 4. A diagram showing the key components of the extended moving-coil loudspeaker driver model.

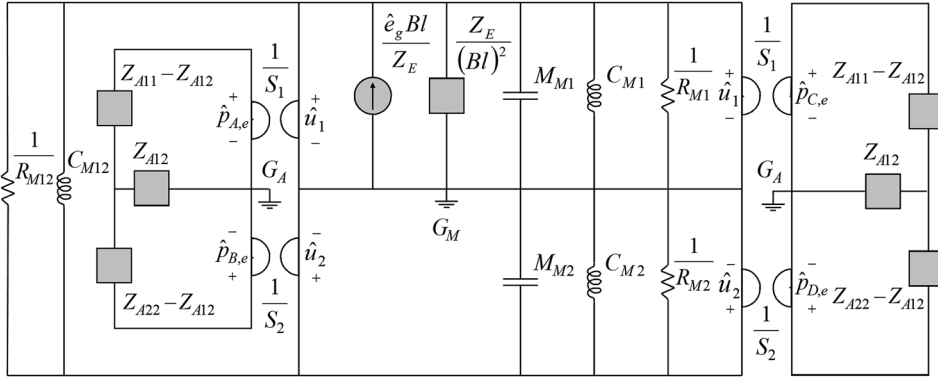


FIG. 5. A multiple-domain analogous circuit representing the extended model shown in Fig. 4. The complex radiating surface velocity amplitudes are uniform and the complex acoustic pressure amplitudes are spatially averaged.

$$Z_{M12} = R_{M12} + \frac{1}{j\omega C_{M12}}. \quad (24)$$

A diagram of the infinite-baffle radiation configuration is shown in Fig. 6. The inner piston (white) of radius a is designated by the number 1 in the following mathematical expressions. The concentric annular piston (shaded) with inner radius a and outer radius b is designated by the number 2. An additional circular piston is required to develop expressions for the radiation impedances. It comprises the areas of both pistons (having a total radius b) and is designated by the number 3.

The self-acoustic impedances of pistons 1 and 3 are well known:²⁷

$$Z_{A11} = \frac{\rho_0 c}{\pi a^2} \left[1 - \frac{J_1(2ka)}{ka} + j \frac{H_1(2ka)}{ka} \right], \quad (25)$$

$$Z_{A33} = \frac{\rho_0 c}{\pi b^2} \left[1 - \frac{J_1(2kb)}{kb} + j \frac{H_1(2kb)}{kb} \right], \quad (26)$$

where J_1 is the first-order Bessel function of the first kind and H_1 is the first-order Struve function. The mutual acoustic impedance between pistons 1 and 2 is^{31–33}

$$Z_{A12} = \frac{\rho_0 c}{\pi a^2} \left[\frac{J_1(2ka)}{ka} - j \frac{H_1(2ka)}{ka} - \frac{e^{-jkb}}{\pi} \int_0^\pi \frac{\sqrt{4\gamma^2 - 4\gamma \cos \theta - \sin^2 \theta}}{\gamma - \cos \theta} e^{jk a \cos \theta} \sin^2 \theta d\theta \right], \quad (27)$$

where $\gamma = b/a$. [The $2\gamma \cos \theta$ in Eqs. (22)–(24) of Ref. 32 should be $4\gamma \cos \theta$ as indicated here.] The self-acoustic impedance of the annular piston is³⁴

$$Z_{A22} = \left(\frac{b^2 Z_{A33} - a^2 Z_{A11} - 2a^2 Z_{A12}}{b^2 - a^2} \right). \quad (28)$$

B. On-axis radiated pressure

The on-axis pressure at an arbitrary distance r from the center of a baffled circular piston of radius a may be expressed as²⁷

$$\hat{p}(r, 0) = j2\rho_0 c \hat{u}_D \sin \left[\frac{k}{2} (\sqrt{r^2 + a^2} - r) \right] e^{-j(k/2)(\sqrt{r^2 + a^2} + r)}. \quad (29)$$

For the extended model, the same expression may be adapted, with changes in variables and superposition, as suggested in Fig. 7. The total on-axis pressure produced by the circular and annular pistons is the sum of the on-axis pressures of the three circular pistons 1, $2a$, and $2b$, with the indicated surface velocities. The uniform velocity \hat{u}_1 of piston 1 represents the motion of the modeled diaphragm. The negative uniform velocity \hat{u}_2 of piston $2a$ plus the positive uniform velocity \hat{u}_2 of piston $2b$ yields the motion of the modeled surround. Both \hat{u}_1 and \hat{u}_2 are solved from the analogous circuit as described earlier. The resulting on-axis pressure is then

$$\hat{p}(r, 0) = j2\rho_0 c \left\{ (\hat{u}_1 - \hat{u}_2) \sin \left[\frac{k}{2} (\sqrt{r^2 + a^2} - r) \right] e^{-j(k/2)(\sqrt{r^2 + a^2} + r)} + \hat{u}_2 \sin \left[\frac{k}{2} (\sqrt{r^2 + b^2} - r) \right] e^{-j(k/2)(\sqrt{r^2 + b^2} + r)} \right\}. \quad (30)$$

IV. EXTENDED-MODEL PARAMETER ESTIMATIONS

While a variety of approaches might be investigated to estimate the extended-model parameters, only one was explored in this work as explained in Secs. IV A–IV E. Results from an actual loudspeaker driver accompany many of the descriptions to highlight several points of interest.

A. Measurement of Bl , Z_E , a , and b

The parameters Bl , Z_E , a , and b may be efficiently estimated using common loudspeaker measurement techniques. (In the following developments, we assume $Z_E \approx R_E + j\omega L_E$.) As suggested in Fig. 2, a vernier scale may be used to estimate the effective radii a and b as half the inner and

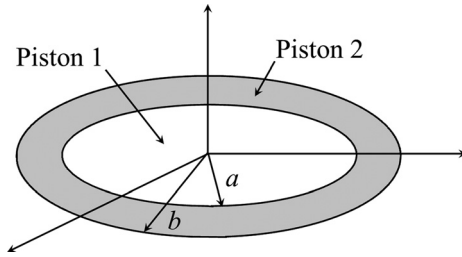


FIG. 6. The basic radiation configuration for a circular piston-like diaphragm (piston 1) and an annular piston-like surround (piston 2).

outer surround diameters, respectively. Another approximation employs the effective radius from the classical model for the circular piston and inner annular piston radii (i.e., $a \rightarrow a_D$). Other techniques, such as those described in Sec. II B, might be explored and adapted to yield more realistic frequency-dependent radii, but such were beyond the scope of this work.

As noted in Sec. II B, a division of the estimated volume velocity by the voice-coil velocity yields an effective area of the diaphragm assembly that is well suited to the classical model. In that case, the velocity \hat{u}_D of the effective piston equals the voice-coil velocity. Another reference velocity (or spatial average of velocities) might also be used^{4,28} with a possible increase in modeling error.

A similar approach might be contemplated to establish the effective areas of the two extended-model pistons. However, the volume velocities of the two regions cannot be readily determined without knowing their areas in advance. Moreover, while the velocity of the central piston might logically correspond to the voice-coil velocity, that of the annular piston would not. For this investigation, we assumed the effective areas and their radii were based on geometrical arguments mentioned earlier in this section. We subsequently assigned effective normal velocities from the spatially averaged axial velocities measured over the two defined regions (see Sec. IV C).

B. SLDV measurement of $\hat{u}_{Sa,i}/\hat{e}_g$

The mechanical parameters M_{M1} , M_{M2} , C_{M1} , C_{M2} , C_{M12} , R_{M1} , R_{M2} , and R_{M12} cannot be measured using existing loudspeaker measurement techniques. However, they can be estimated by curve fitting the theoretical velocity FRFs \hat{u}_1/\hat{e}_g and \hat{u}_2/\hat{e}_g in Eqs. (17) and (18) to corresponding measured velocity FRFs. Evaluations of many discrete $\hat{u}_{Sa,i}/\hat{e}_g$ were made using a broadband random-noise excitation signal and a Polytec PSV-400 SLDV in an anechoic chamber. As

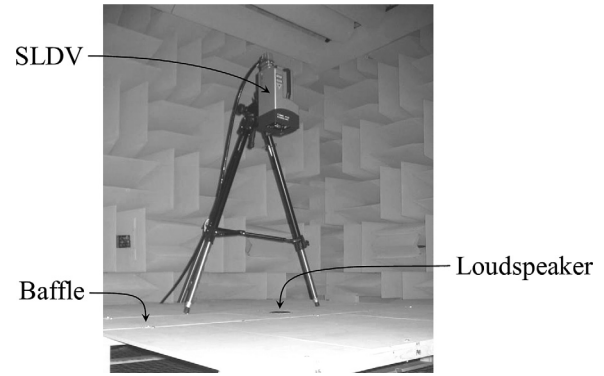


FIG. 8. An SLDV measurement setup for a loudspeaker mounted in a $2.5 \text{ m} \times 2.5 \text{ m}$ baffle within an anechoic chamber.

shown in Fig. 8, each loudspeaker was mounted in a $2.5 \text{ m} \times 2.5 \text{ m}$ baffle (larger than that specified in Ref. 13) raised 0.3 m off the cable floor to simulate the desired radiation condition. The baffle was constructed using several rabbeted sections of 1.3 cm thick medium-density fiberboard, forming a surface that was reasonably airtight and smooth. The SLDV head was positioned directly above the loudspeaker with a standoff distance of 1.2 m. Because the combined mass of the driver magnet, frame, baffle structure, SLDV tripod, and SLDV head was several orders of magnitude greater than that of the loudspeaker diaphragm, the driver reaction force produced negligible acceleration of the measurement system.

Over 400 scan points were used to thoroughly characterize the vibrational properties of each driver and produce reliable spatially averaged values. As shown in the typical scan-point grid of Fig. 9, the majority of points were located on the diaphragm, but many were also located on the surround. Other authors have used similar patterns.^{4,35} Rectilinear, honeycomb, and radial grid patterns were all investigated, but because of the circular driver geometries, the radial grid pattern provided the most efficient means of separating the measured scan points into diaphragm and surround regions.

C. Estimation of \hat{u}_1/\hat{e}_g and \hat{u}_2/\hat{e}_g through spatial averaging of $\hat{u}_{Sa,i}/\hat{e}_g$

While the extended model assumes the diaphragm and surround vibrate uniformly over their respective surface areas S_1 and S_2 , the two elements fail to satisfy this ideal exactly—even below their breakup frequencies. Spatial averages of the

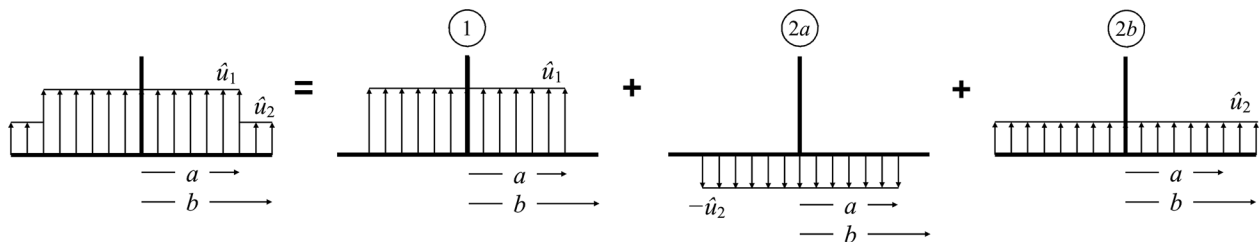


FIG. 7. The vibrational superposition of three baffled circular pistons to produce the on-axis pressure of a single circular piston (diaphragm) with velocity amplitude \hat{u}_1 and a concentric annular piston (surround) with velocity amplitude \hat{u}_2 .

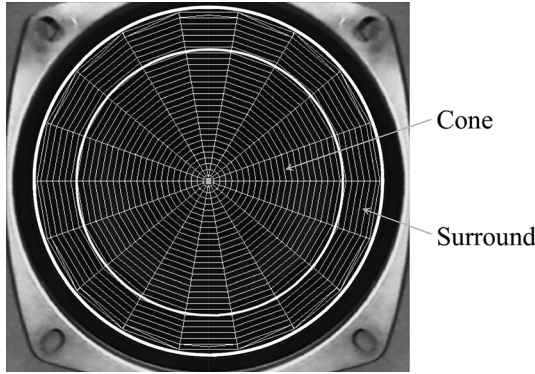


FIG. 9. An example of a radial SLDV scan-point grid for a baffled loudspeaker. The diaphragm and surround boundaries have been superimposed on the image for clarity.

various $\hat{u}_{Sa,i}/\hat{e}_g$ over the regions were accordingly used to better associate the measured data with the modeled effective piston vibrations and thus provide more useful results for parameter extractions. (This approach was also in accordance with the concepts discussed in Sec. II B.) Examples of the real and imaginary parts of $\langle \hat{u}_{Sa,i}/\hat{e}_g \rangle_{S_1}$ and $\langle \hat{u}_{Sa,i}/\hat{e}_g \rangle_{S_2}$ are shown in Fig. 10 for a Radio Shack (RS) 40-1197 (FE-103), a driver believed to have interesting surround-related properties from previous observations in active sound transmission control experiments.^{36,37}

D. Determination of the secondary resonance frequency f_2

Identification of the secondary resonance frequency f_2 is another important step in the parameter estimation process. It serves as a constraint in the curve-fitting routine described in Sec. IV E, requiring the model to have the same resonance frequency. A resonance frequency occurs when the imaginary part of $\langle \hat{u}_{Sa,i}/\hat{e}_g \rangle_{S_1}$ or $\langle \hat{u}_{Sa,i}/\hat{e}_g \rangle_{S_2}$ becomes zero.³⁸ The primary frequency f_1 is readily ascertained in Fig. 10 (near 110 Hz), but f_2 is not. The mode indicator function (MIF)³⁹ given by the expression

$$\text{MIF}_n = \frac{\text{Im}\{\langle \hat{u}_{Sa,i}/\hat{e}_g \rangle_{S_n}\}}{|\langle \hat{u}_{Sa,i}/\hat{e}_g \rangle_{S_n}|} \quad (31)$$

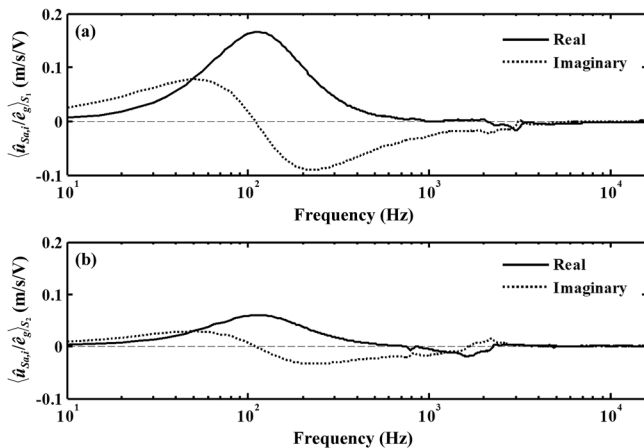


FIG. 10. Spatially averaged velocity FRFs for an RS 40-1197 (FE-103) loudspeaker. (a) Diaphragm. (b) Surround.

was accordingly used to better identify both frequencies, where $n=1$ for the diaphragm and $n=2$ for the surround. When the MIF is plotted on a log-log scale, resonances appear as pronounced dips, making their frequencies much more discernible. This again follows from the fact that the imaginary part of an FRF passes through zero at a resonance, while its magnitude remains relatively large.

In theory, both the diaphragm and surround should have two notches in their respective MIFs, at both resonance frequencies of the two-degree-of-freedom system. However, the observability depends strongly upon the relative values of M_{M1} and M_{M2} . If M_{M1} is much larger than M_{M2} (e.g., if $M_{M1}/M_{M2} > 100$), MIF_1 does not exhibit an appreciable dip at the second resonance frequency. This behavior also depends to a lesser extent on mechanical compliance and resistance values.

The MIFs for the RS 40-1197 (FE-103) (with a mass ratio $M_{M1}/M_{M2} \approx 101$) are shown in Fig. 11. They demonstrate that the diaphragm and surround undergo a mutual resonance near 110 Hz, but only the surround exhibits an appreciable resonance near 1.67 kHz. One might accordingly refer to the second resonance as the “surround resonance.” The MIF patterns were similar for all other drivers tested in the investigation; their mass ratios were even larger.

As an additional step, MIF_2 may be divided by MIF_1 to produce a curve more clearly accentuating resonances that are not mutual. Because the first prominent dip would then correspond to the surround resonance frequency, the quotient might be termed the surround resonance indicator function (SRIF):

$$\text{SRIF} = \frac{\text{MIF}_2}{\text{MIF}_1}. \quad (32)$$

The SRIF for the same driver is shown in Fig. 12. Once again, the surround resonance frequency is found near 1.67 kHz. As verified through SLDV operating deflection shapes (ODSs),⁴⁰ the surround exhibited nearly uniform

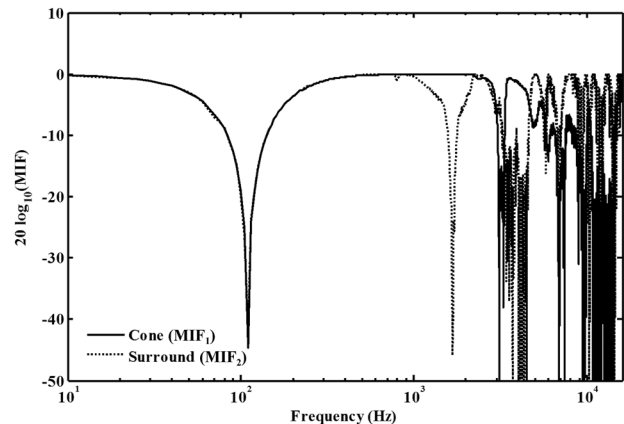


FIG. 11. The MIFs for the diaphragm and surround of an RS 40-1197 (FE-103) loudspeaker. The first dip at 110 Hz corresponds to the primary resonance frequency f_1 , which is common to both the diaphragm and surround. The second dip at 1.67 kHz corresponds to the secondary resonance frequency f_2 , which is significant only for the surround. Although the latter is theoretically the second diaphragm/surround system resonance frequency, it may be loosely termed the “surround resonance frequency.” Dips above 2 kHz correspond to frequencies of diaphragm and surround breakup.

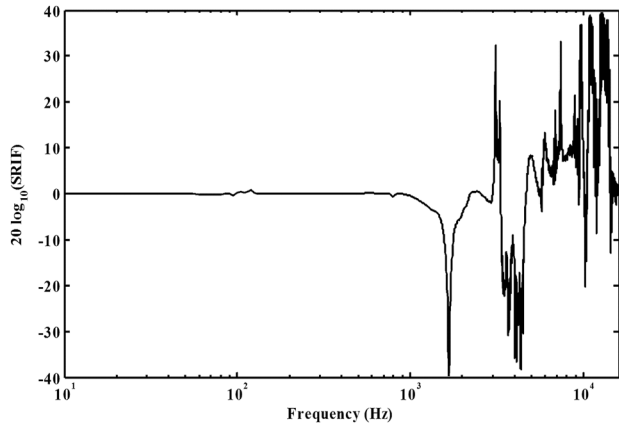


FIG. 12. The SRIF for the RS 40-1197 (FE-103) loudspeaker. The first prominent dip at 1.67 kHz corresponds to the surround resonance frequency. Higher-frequency peaks and dips ostensibly represent independent diaphragm and surround breakup resonance frequencies, respectively.

out-of-phase motion with that of the diaphragm over a limited bandwidth about this frequency. An example is shown in Fig. 13. This behavior was consistent for all drivers tested in the investigation; several additional SRIF graphs and color ODS images are available in Ref. 11.

The distinct peaks and dips above 2 kHz in Fig. 12 correspond to frequencies of diaphragm and surround breakup, which no longer satisfy the lumped-parameter model assumptions. However, in this spectral region, the SRIF may still be useful to identify independent breakup resonances. In principle, independent diaphragm resonances should peak, while independent surround resonances should dip in the plot.

E. Curve fitting to estimate the parameters M_{M1} , M_{M2} , C_{M1} , C_{M2} , C_{M12} , R_{M1} , R_{M2} , and R_{M12}

The constrained nonlinear minimization function `fmincon` of the MATLAB Optimization Toolbox (The MathWorks,

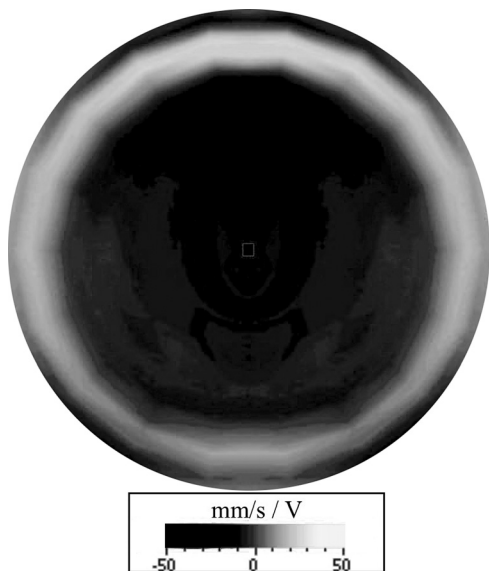


FIG. 13. The ODS of the RS 40-1197 (FE-103) cone and surround at the surround resonance frequency of 1.67 kHz.

Inc., Natick, MA) was used to extract the unknown extended-model parameters from the measured data. It incorporated a fitness function F , defined by the authors, to minimize the sum of the squared error (SSE) between the real and imaginary parts of the measured, spatially averaged FRFs $\langle \hat{u}_{Sa,i} / \hat{e}_g \rangle_{S_n}$ and those of the predicted, uniform FRFs \hat{u}_n / \hat{e}_g :

$$F = \frac{1}{4} \sum_l \left\{ \left[\text{Re} \left(\left\langle \frac{\hat{u}_{a,i}}{\hat{e}_g} \right\rangle_{S_1} \right) - \text{Re} \left(\frac{\hat{u}_1}{\hat{e}_g} \right) \right]^2 + \left[\text{Im} \left(\left\langle \frac{\hat{u}_{a,i}}{\hat{e}_g} \right\rangle_{S_1} \right) - \text{Im} \left(\frac{\hat{u}_1}{\hat{e}_g} \right) \right]^2 + \left[\text{Re} \left(\left\langle \frac{\hat{u}_{a,i}}{\hat{e}_g} \right\rangle_{S_2} \right) - \text{Re} \left(\frac{\hat{u}_2}{\hat{e}_g} \right) \right]^2 + \left[\text{Im} \left(\left\langle \frac{\hat{u}_{a,i}}{\hat{e}_g} \right\rangle_{S_2} \right) - \text{Im} \left(\frac{\hat{u}_2}{\hat{e}_g} \right) \right]^2 \right\}. \quad (33)$$

The summation over all discrete measurement frequencies is denoted by the index l . As clarified in the `fmincon` documentation, the routine was able to constrain the resonance frequency f_2 of the modeled driver to match that of the measured driver indicated by the SRIF. It also constrained all parameter values to be greater than zero. Because `fmincon` requires initial guesses for the values, the parameters M_{MD} , C_{MS} , and R_{MS} were used as guesses for the related parameters M_{M1} , M_{M2} , C_{M1} , C_{M2} , C_{M12} , R_{M1} , R_{M2} , and R_{M12} . While these assignments were arbitrary, upper and lower bounds were placed on the allowed values, with some relaxation in the event that they became binding during the fit.

The extracted parameter values for the RS 40-1197 (FE-103) loudspeaker are shown in Table I, along with other conventionally measured linear parameters. The values for Bl , L_E , and R_E were used as known values in the extraction process. The resulting diaphragm velocity FRFs from the classical and extended models are compared to the measured spatially averaged velocity FRF in Fig. 14. The quality of the extended-model fit is clearly superior. The curve-fitted surround velocity FRF from the extended model is compared to the measured spatially averaged FRF in Fig. 15. Again, the quality of the fit is very good. However, because the

TABLE I. Conventionally measured parameters and extracted extended-model parameters for the RS 40-1197 (FE-103) loudspeaker.

Conventionally measured parameters			Extracted extended-model parameters		
Parameter	Value	Units	Parameter	Value	Units
Bl	4.65	Tm	M_{M1}	3.00	g
C_{MS}	0.000752	m/N	M_{M2}	0.0296	g
f_1	117	Hz	C_{M1}	0.00250	m/N
L_E	0.161	mH	C_{M2}	0.000294	m/N
M_{MD}	2.45	g	C_{M12}	0.000534	m/N
R_{MS}	0.442	kg/s	R_{M1}	0.676	kg/s
R_E	7.65	Ω	R_{M2}	0.160	kg/s
S_D	47.8	cm ²	R_{M12}	0.0558	kg/s

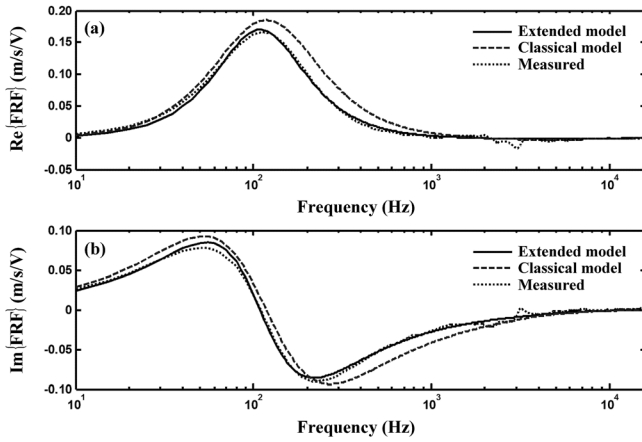


FIG. 14. Fitted extended-model prediction, linear-parameter classical-model prediction, and spatially averaged measured velocity FRF for the RS 40-1197 (FE-103) loudspeaker diaphragm. (a) Real part. (b) Imaginary part.

classical model fails to predict a distinct surround vibration, an associated curve is not included in the figure.

As with most multi-parameter curve-fitting processes, there is no guarantee that this approach produces a unique solution set. However, to increase confidence in its feasibility, the process was repeated with several other initial guesses. In each case, the final parameter values were nearly identical, falling within a few percent of one another. Additional support came from the fact that the extracted values were on the same order of magnitude as the conventional values. Nevertheless, the approach provides only one example of how the parameters might be estimated. Other methods that substantiate unique values require further investigation.

F. Extended-model parameters for seven loudspeakers

The methods described in Secs. IV A–IV E were also used to determine the parameters of six additional loudspeakers as shown Table II. The smallest was a HiVi A2S ($a \approx 2.0$ cm) and the largest was a Fostex prototype ($a \approx 8.1$ cm). Two general trends are apparent from the data.

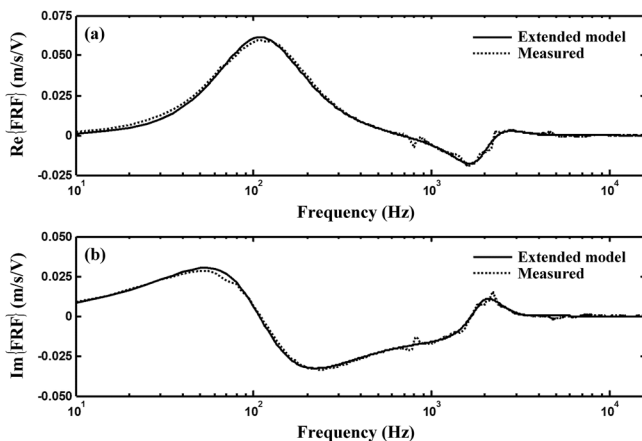


FIG. 15. Fitted extended-model prediction and spatially averaged measured velocity FRF for the RS 40-1197 (FE-103) loudspeaker surround. (a) Real part. (b) Imaginary part.

First, the extracted mass M_{M1} of the diaphragm is consistently much larger than the mass M_{M2} of the surround and slightly larger than the classical mass M_{MD} . Second, the extracted compliance C_{M1} of the spider is consistently much larger than the isolated compliances C_{M12} and C_{M2} of the surround.

V. ACOUSTICAL VALIDATION

Because the extended model parameters could not be checked against published values and other estimation techniques have not been developed, an acoustical method was used as a means of validation. The approach is based on the formulations in Sec. III B and is described in Secs. V A and V B.

A. Measurement configuration

The FRF between the input voltage to each loudspeaker and its on-axis pressure was measured in the anechoic chamber using the same baffle and broadband random noise excitation used for the SLDV scans. Both sets of measurements were conducted over a 4 h period with a thermostat set point of 22.5°C . Other ambient conditions and variations in conditions were not considered. A precision free-field microphone was calibrated prior to each measurement and positioned on axis to detect the radiated pressure. Coherence values greater than 0.98 were achieved at all frequencies between 50 Hz and 10 kHz. Equation (30) was used to estimate the axial distances required for the pressure magnitude to exhibit $1/r$ dependence in this bandwidth. A microphone distance of $r = 23$ cm was found to be satisfactory for all loudspeakers except the Fostex driver, which had an upper limit of roughly 5 kHz at this distance.

While r might have been larger, it was desirable to keep it as small as possible, while still maintaining this particular far-field condition. Interference due to diffraction from the rear of the loudspeaker, around the finite-dimension baffle, and to the microphone position became more pronounced as r increased. These effects were also more severe at lower frequencies and were consistent for all loudspeakers. Olson⁴¹ observed similar effects and suggested that an “irregular” baffle could reduce the diffraction interference. This might be realized by mounting the loudspeaker off center, changing the baffle shape, or both.¹³ Interference would still occur, but with more diversified path lengths, the effects would tend to smear over wider spectral bands, causing the FRFs to become smoother. After experimenting with several configurations, the validation measurements were taken with the loudspeaker 45 cm off center and a small corner baffle section removed. Additional details are provided elsewhere.¹¹

B. Measurement and modeling results

Of the various loudspeakers listed in Table II, the AuraSound NS3 8D produced one of the most substantial surround dips in its on-axis pressure FRF. Figure 16 shows the measured result, along with predictions from the classical and extended models. The surround dip occurs near 5 kHz.

TABLE II. Conventionally measured parameters and extracted extended-model parameters for seven loudspeakers: (1) HiVi A2S, (2) AuraSound NS3 8D, (3) Audax HP100MO, (4) RS 40-1197 (FE-103), (5) HiVi M4N, (6) AuraSound NS4 8A, and (7) Fostex prototype.

Parameter	Loudspeaker number							Units
	1	2	3	4	5	6	7	
a	2.00	3.10	3.90	4.00	4.15	4.20	8.05	cm
b	2.20	3.50	4.35	4.55	4.55	4.60	8.90	cm
Bl	2.97	3.65	5.44	4.65	3.54	3.51	11.2	Tm
C_{M1}	0.000899	0.00145	0.00111	0.00250	0.00240	0.00550	0.00250	m/N
C_{M2}	0.000101	0.00040	0.00030	0.00029	0.00046	0.00038	0.000185	m/N
C_{M12}	0.000202	0.00023	0.00026	0.00053	0.00028	0.00043	0.0000784	m/N
C_{MS}	0.000164	0.00055	0.00042	0.00075	0.00067	0.00089	0.000333	m/N
L_E	0.108	0.154	0.173	0.161	0.230	0.165	0.682	mH
M_{M1}	2.82	2.28	6.40	3.00	6.51	3.66	54.5	g
M_{M2}	0.00280	0.00450	0.0170	0.0296	0.00340	0.0327	0.368	g
M_{MD}	2.53	2.11	4.87	2.45	5.43	3.00	39.1	g
R_E	6.32	6.76	5.82	7.65	6.48	7.25	6.59	Ω
R_{M1}	0.619	0.339	1.137	0.676	0.483	0.412	0.426	kg/s
R_{M2}	0.232	0.00210	0.257	0.160	0.0330	0.159	3.26	kg/s
R_{M12}	0.0707	0.00490	0.0495	0.0558	0.00100	0.0600	2.31	kg/s
R_{MS}	0.758	0.621	1.08	0.441	0.509	0.432	2.53	kg/s

While the classical model is not capable of predicting the anomaly, the extended model predicts it reasonably well. Of course, neither is able to predict irregularities due to diaphragm or surround breakup at higher frequencies. Baffle diffraction effects are also present in the measured data while being absent in the modeled FRFs. Nevertheless, the classical and extended models both produce reasonable agreement at low frequencies. Only the extended model provides a useful characterization through the surround dip region.

Figure 17 shows the measured response of the RS 40-1197 (FE-103) driver, along with the model predictions. The extended model successfully predicts the dip near 2 kHz, but because the measured response is affected by a strong diaphragm breakup resonance near 3 kHz (see Fig. 12), it does not match as well as it might have otherwise. The model excels at estimating the response magnitude up to the surround resonance frequency f_2 .

Some loudspeakers did not manifest substantial surround dips (measured or predicted) in their on-axis pressure

FRFs. Although surround resonances were consistently detected through SLDV scans and resulting SRIFs, their acoustic effects were sometimes limited, such that the response dips remained small or negligible. Nevertheless, the extended model remained successful in the sense that it accurately predicted these behaviors and consistently provided better response predictions up to f_2 .

To better quantify the improvements, linear-scale SSEs were computed between the predicted and measured on-axis pressure FRFs for each loudspeaker, with the upper frequency limit set to f_2 in each case. The percent reduction in error between the classical and extended models was subsequently calculated as

$$\text{PRE} = 100 \left(\frac{\text{SSE}_c - \text{SSE}_e}{\text{SSE}_c} \right). \quad (34)$$

The surround resonance frequency, model SSEs, and PRE are presented in Table III for each loudspeaker. Notable error reductions occurred in every case, suggesting that the

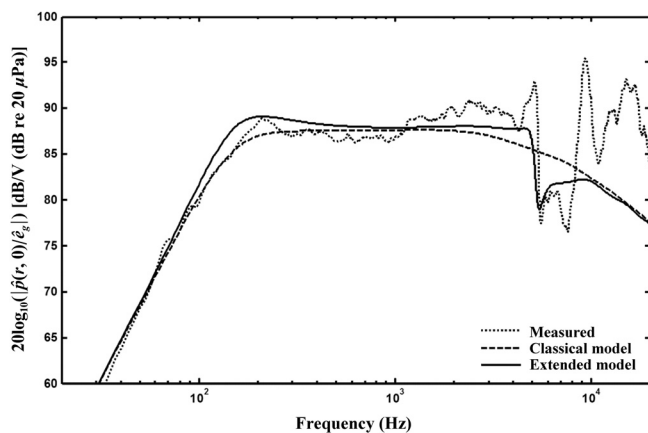


FIG. 16. Measured and modeled on-axis pressure FRFs for the AuraSound NS3 8D loudspeaker at $r = 23$ cm.

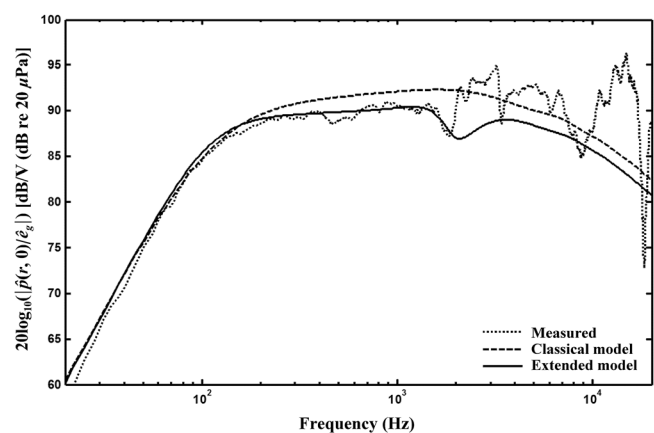


FIG. 17. Measured and modeled on-axis pressure FRFs for the RS 40-1197 (FE-103) loudspeaker at $r = 23$ cm.

TABLE III. Surround resonance frequencies, sums of squared errors (for the on-axis response predictions of the classical and extended models), and percent reductions in error (between the two models) for seven loudspeakers: (1) HiVi A2S, (2) AuraSound NS3 8D, (3) Audax HP100MO, (4) RS 40-1197 (FE-103), (5) HiVi M4N, (6) AuraSound NS4 8A, and (7) Fostex prototype.

Measure	Loudspeaker number							Units
	1	2	3	4	5	6	7	
f_2	9105	3920	2310	1670	3430	1680	1440	Hz
SSE _c	23.0	22.9	16.8	11.6	1.40	6.70	12.0	Pa ² /V ²
SSE _e	13.1	13.7	1.70	0.60	1.10	1.70	2.40	Pa ² /V ²
PRE	43.0	40.2	89.9	94.6	21.4	74.6	80.0	%

extended model and parameter extraction technique consistently provided better overall predictions of the baffled on-axis responses than the classical approach.

VI. CONCLUSIONS

This paper has explored a straightforward extension of the classical lumped-element model of a moving-coil loudspeaker and demonstrated its potential to improve radiated acoustic response predictions. It does so by incorporating additional lumped elements that better represent the distinct contributions of the diaphragm and surround, while isolating the roles of the spider and surround in the suspension system. Experimental results have verified its capabilities for several baffled loudspeakers from very low frequencies through their primary and secondary (surround) resonance frequencies. It extends the effective prediction bandwidth to mid frequencies, while better characterizing loudspeaker responses with or without notable surround dips. It also provides insights into their distinctions that may be used to troubleshoot and improve driver performance characteristics.

Because the model does not predict higher-order interactions and modal behaviors of diaphragms and surrounds, its benefits are inherently limited. However, it remains a functional tool that can easily integrate with current loudspeaker design methods. If properly used, it may assist loudspeaker designers to better simulate general loudspeaker responses and systematize alterations to diaphragms, surrounds, and spiders with the aim of improving those responses. It may also help substantiate the presumed properties of high or low-quality drivers.

For the model to be successful, its parameters must be appropriately estimated for a given driver. This paper has introduced one estimation technique involving the use of an SLDV to measure velocity frequency response functions at several diaphragm and surround positions. Their spatial averages were used with a constrained optimization routine to estimate the model parameter values. The paper has introduced an SRIF that easily identifies the surround resonance frequency to help constrain the routine. Other approaches, including curve fitting of driver electric input impedances or other measured values, might be explored to determine the distinct parameters more uniquely. A method that better predicts the frequency-dependent effective

radiating areas of the diaphragm and surround would also be beneficial.

The developments have assumed the self and mutual radiation impedances on the front and back sides of a baffled loudspeaker are equal. This cannot be strictly true because the coil former, spider, magnet structure, and frame are not completely unobtrusive. Moreover, in practical cases, a driver is mounted on an enclosure with a distinct rear loading. Complete system models must be adapted to these conditions, but if the driver parameters have been successfully established through initial measurements, system performance results should be predictable. The authors encourage research in these and other areas to refine the proposed model and improve its utility.

LIST OF SYMBOLS

a	Radius of a diaphragm, circular piston, inner surround perimeter, or inner annular piston perimeter
a_b	Base radius of a right circular cone
a_D	Effective radius of a diaphragm assembly
b	Total radius of a diaphragm and surround, outer surround perimeter, or outer annular piston perimeter
Bl	Force factor
c	Speed of sound in air, ≈ 343 m/s
C_{Mn}	Effective mechanical compliance of the n th suspension element (extended model)
C_{Mmn}	Effective mechanical compliance coupling the m th and n th radiating surfaces ($m \neq n$) (extended model)
C_{MS}	Effective mechanical compliance of the suspension (classical model)
\hat{e}_g	Complex open-circuit voltage amplitude of the signal generator
F	Fitness function for the curve-fitting routine
f	Frequency
f_n	n th resonance frequency of the diaphragm/surround system ($n=2$ for the surround resonance frequency)
FRF	Frequency response function
G_A	Acoustic ground (ambient reference pressure)
$G_{hs}(\mathbf{r} \mathbf{r}_S)$	Half-space time-harmonic Green's function
G_M	Mechanical ground (zero reference velocity)
h	Height of a right circular cone
$H(f)$	Volume velocity FRF (transfer function), $= \hat{U}/\hat{e}_g$
H_1	First-order Struve function
$H_i(f)$	Axial surface velocity FRF (transfer function) for the i th discrete measurement position, $= \hat{u}_{Sa,i}/\hat{e}_g$
h_s	Slant height of a right circular cone
i	Integer index value
I	Upper limit for i
j	$\sqrt{-1}$, integer index value
J_n	n th-order Bessel function of the first kind

k	Acoustic wave number, $= \omega/c$	S	Surface area
l	Index value for discrete measurement frequencies	S_D	Effective radiating area of the diaphragm assembly (classical model), $= \pi a_D^2$
L_E	Effective electric inductance of the voice coil	S_n	Effective area of the n th radiating surface (extended model)
m	Integer index value representing a driver element, $= 1$ or 2	SRIF	Surround resonance indicator function
MIF_n	Mode indicator function for the n th radiating surface	SSE	Sum of the squared error
M_{MD}	Effective mechanical mass (classical model)	SSE_c	Sum of the squared error for the classical model
M_{Mn}	Effective mechanical mass of the n th radiating surface (extended model)	SSE_e	Sum of the squared error for the extended model
n	Integer index value representing a driver element, $= 1$ or 2 (or 3 for radiation impedance calculations)	\hat{U}	Complex volume velocity amplitude
\mathbf{n}_S	Unit vector normal to the surface S	$\hat{\mathbf{u}}_i$	Complex particle velocity amplitude vector, assumed to be uniform over ΔS_i
$\mathbf{n}_{S,i}$	Unit vector normal to the surface element ΔS_i	$\hat{\mathbf{u}}(\mathbf{r}_S)$	Complex particle velocity amplitude vector at \mathbf{r}_S
$\hat{p}(\mathbf{r})$	Complex acoustic pressure amplitude at \mathbf{r}	\hat{u}_D	Complex normal velocity amplitude of an effective piston representing the diaphragm assembly (classical model)
$\hat{p}(r, \theta)$	Axisymmetric complex acoustic pressure amplitude at distance r and angle θ	\hat{u}_n	Complex normal velocity amplitude of the n th effective piston representing a radiating area of the diaphragm assembly (extended model)
$\hat{p}(r, 0)$	On-axis complex acoustic pressure amplitude at distance r	$\hat{u}_{n,i}$	Complex normal particle velocity amplitude for the i th discrete measurement position, $= \hat{u}_i \cos \theta_i$
$\hat{p}_{A,c}$	Complex (spatially averaged) acoustic pressure amplitude on the back of the diaphragm assembly (classical model)	$\hat{\mathbf{u}}_S(\mathbf{r}_S)$	Complex surface velocity amplitude vector at \mathbf{r}_S
$\hat{p}_{A,e}$	Complex (spatially averaged) acoustic pressure amplitude on the back of the diaphragm (extended model)	\hat{u}_{Sa}	Complex axial surface velocity amplitude
$\hat{p}_{B,c}$	Complex (spatially averaged) acoustic pressure amplitude on the front of the diaphragm assembly (classical model)	$\hat{u}_{Sa,i}$	Complex axial surface velocity amplitude for the i th discrete measurement position
$\hat{p}_{B,e}$	Complex (spatially averaged) acoustic pressure amplitude on the back of the surround (extended model)	$u_{Sn}(\mathbf{r}_S)$	Normal surface velocity amplitude at \mathbf{r}_S (time domain)
$\hat{p}_{C,e}$	Complex (spatially averaged) acoustic pressure amplitude on the front of the diaphragm (extended model)	$\hat{u}_{Sn}(\mathbf{r}_S)$	Complex normal surface velocity amplitude at \mathbf{r}_S (frequency domain)
$\hat{p}_{D,e}$	Complex (spatially averaged) acoustic pressure amplitude on the front of the surround (extended model)	V_{AS}	Volume of air having the same acoustic compliance as the driver suspension, $= \rho_0 c^2 C_{MS} S_D^2$
PRE	Percent reduction in error	$V(t)$	Time-varying volume displacement of a diaphragm assembly
Q_p	Directivity factor of a diaphragm assembly along its principal axis	W	Sound power
\mathbf{r}	Position vector from the origin to the field (observation) point	z	Displacement from the (assumed) radiating plane along the principal loudspeaker axis (coordinate axis)
r	Radial distance from the origin to the field point, $= \mathbf{r} $	Z_{Ann}	Self-acoustic impedance of the n th radiating surface, modeled as a circular or annular piston in an infinite plane rigid baffle (extended model)
\mathbf{r}_S	Position vector from the origin to a point on a surface	Z_{Ann}	Mutual acoustic impedance between the m th and n th radiating surfaces ($m \neq n$), modeled as a circular piston m and a concentric annular piston n in an infinite plane rigid baffle (extended model)
r_S	Radial distance from the origin to a point on a surface, $= \mathbf{r}_S $	Z_{AR}	Acoustic radiation impedance of the diaphragm assembly, modeled as a circular piston in an infinite plane rigid baffle (classical model)
R	Distance between a surface point and a field point, $= \mathbf{r} - \mathbf{r}_S $	Z_E	Blocked electric impedance, $\approx R_E + j\omega L_E$
R_E	Electric resistance of the voice coil	Z_{M1}	Mechanical impedance substitution (extended model)
R_{Mn}	Effective mechanical resistance of the n th suspension element (extended model)	Z_{M2}	Mechanical impedance substitution (extended model)
R_{Mmn}	Effective mechanical resistance coupling the m th and n th radiating surfaces ($m \neq n$) (extended model)	Z_{M12}	Mechanical impedance substitution (extended model)
R_{MS}	Effective mechanical resistance of the suspension (classical model)	Z_{MA}	Mechanical impedance substitution (extended model)
		Z_{MB}	Mechanical impedance substitution (extended model)

Z_{MC}	Mechanical impedance substitution (extended model)
Z_{MR}	Mechanical radiation impedance of the diaphragm assembly, modeled as a circular piston in an infinite plane rigid baffle (classical model)
$z_S(t)$	Time-varying axial displacement of an idealized diaphragm surface
α	Cone semi-apex angle
γ	Ratio of radii, $= b/a$
ΔS_i	i th discrete surface element
θ	Angle between \mathbf{r} and the axis of a baffled right circular cone or transformation variable from Ref. 31
θ_i	Angle between $\hat{\mathbf{u}}_i$ and \mathbf{n}_{S_i}
λ	Acoustic wavelength, $= c/f$
ρ_0	Ambient density of air, $\approx 1.21 \text{ kg/m}^3$
ω	Angular frequency, $= 2\pi f$
$\langle \dots \rangle_S$	Spatial average over the surface S
$\langle \dots \rangle_{S,w}$	Weighted spatial average over the surface S
$\langle \dots \rangle_{S,t}$	Spatial and time average over the surface S
$\langle \dots \rangle_t$	Time average

¹L. L. Beranek, *Acoustics* (Acoustical Society of America, New York, 1986), pp. 183–188, 191–192, 199–202, 231.

²R. H. Small, “Direct-radiator loudspeaker system analysis,” *J. Audio Eng. Soc.* **20**, 383–395 (1972).

³J. N. Moreno, R. A. Moscoso, and S. Jönsson, “Measurement of the effective radiating surface area of a loudspeaker using a laser velocity transducer and a microphone,” 96th Conv. Audio Eng. Soc., Preprint 3861 (1994).

⁴W. Klippel and J. Schlechter, “Dynamic measurement of transducer effective radiation area,” *J. Audio Eng. Soc.* **59**, 44–52 (2011).

⁵H. F. Olson, J. Preston, and E. G. May, “Recent developments in direct-radiator high-fidelity loudspeakers,” *J. Audio Eng. Soc.* **2**, 219–227 (1954).

⁶J. Eargle, *Loudspeaker Handbook*, 2nd ed. (Kluwer, Boston, 2003), pp. 30–31.

⁷P. Newell and K. Holland, “Diversity of design: Loudspeakers by Philip Newell and Keith Holland,” in *Audio Engineering Explained—Professional Audio Recording*, edited by D. Self (Focal Press, Oxford, 2010), Chap. 12, pp. 357–358.

⁸T. W. Leishman and J. Tichy, “A theoretical and numerical analysis of vibration-controlled modules for use in active segmented partitions,” *J. Acoust. Soc. Am.* **118**, 1424–1438 (2005).

⁹J. D. Sagers, T. W. Leishman, and J. D. Blotter, “A double-panel active segmented partition module using decoupled analog feedback controllers: Numerical model,” *J. Acoust. Soc. Am.* **125**, 3806–3818 (2009).

¹⁰R. J. True, “The dominant compliance of loudspeaker drivers,” SAE International Congress and Exposition, Detroit, SAE Technical Paper 910651 (1991).

¹¹J. D. Sagers, “Analog Feedback Control of an Active Sound Transmission Control Module,” M.S. thesis, Brigham Young University, Provo, UT (2008), Chap. 4. Available online through Brigham Young University Electronic Theses & Dissertations at <<http://etd.lib.byu.edu>> (Last viewed July 5, 2013).

¹²J. D. Sagers, T. W. Leishman, and J. D. Blotter, “Active sound transmission control of a double-panel module using decoupled analog feedback control: Experimental results,” *J. Acoust. Soc. Am.* **128**, 2807–2816 (2010).

¹³IEC 60268-5, *Sound System Equipment—Part 5: Loudspeakers*, 3rd ed. (International Electrotechnical Commission, Geneva, Switzerland, 2003).

¹⁴F. J. M. Frankort, “Patterns and radiation behavior of loudspeaker cones,” *J. Audio Eng. Soc.* **26**, 609–622 (1978).

¹⁵T. Shindo, O. Yashima, and H. Suzuki, “Effect of voice-coil and surround on vibration and sound pressure response of loudspeaker cones,” *J. Audio Eng. Soc.* **28**, 490–499 (1980).

¹⁶D. A. Barlow, G. D. Galletly, and J. Mistry, “The resonances of loudspeaker diaphragms,” *J. Audio Eng. Soc.* **29**, 699–704 (1980).

¹⁷M. S. Corrington and M. C. Kidd, “Amplitude and phase measurements on loudspeaker cones,” *Proc. IRE* **39**, 1021–1026 (1951).

¹⁸K. Suzuki and I. Nomoto, “Computerized analysis and observation of the vibration modes of a loudspeaker cone,” *J. Audio Eng. Soc.* **30**, 98–106 (1982).

¹⁹W. M. Leach, Jr., *Introduction to Electroacoustics and Audio Amplifier Design*, 4th ed. (Kendall Hunt, Dubuque, IA, 2010), pp. 89–94.

²⁰J. A. D’Appolito, *Testing Loudspeakers* (Audio Amateur Press, Peterborough, NH, 1998), Chaps. 2, 3, and 7.

²¹L. L. Beranek and T. J. Mellow, *Acoustics: Sound Fields and Transducers* (Academic Press, London, 2012), Sec. 4.16, Chap. 6.

²²A. D. Pierce, *Acoustics: An Introduction to its Physical Principles and Applications* (Acoustical Society of America, New York, 1989), Secs. 4–6 and 5–2, pp. 320–321.

²³E. G. Williams, *Fourier Acoustics: Sound Radiation and Nearfield Acoustical Holography* (Academic Press, London, 1999), Sec. 2.10, Chap. 8.

²⁴W. N. Brown, Jr., “Theory of conical sound radiators,” *J. Acoust. Soc. Am.* **13**, 20–22 (1941).

²⁵P. G. Bordonio, “The conical sound source,” *J. Acoust. Soc. Am.* **17**, 123–126 (1945).

²⁶F. J. M. Frankort, “Vibration and sound radiation of loudspeaker cones,” Ph.D. dissertation, Delft University of Technology, Delft, The Netherlands (1975) [reprinted in Philips Res. Rep., Suppl. No. 2, pp. 1–189 (1975)], pp. 110–125.

²⁷L. E. Kinsler, A. R. Frey, A. B. Coppens, and J. V. Sanders, *Fundamentals of Acoustics*, 4th ed. (Wiley, New York, 2000), pp. 179–181, 186.

²⁸D. K. Anthony and S. J. Elliott, “A comparison of three methods of measuring the volume velocity of an acoustic source,” *J. Audio Eng. Soc.* **39**, 355–366 (1991).

²⁹S. Jönsson, “Accurate determination of loudspeaker parameters using audio analyzer type 2012 and laser velocity transducer type 3544,” Brüel and Kjær Application Note BO 0384-12 (1996).

³⁰C. H. Hansen and S. D. Snyder, *Active Control of Noise and Vibration* (E & FN Spon, London, 1997), pp. 117–118.

³¹P. R. Stepanishen, “The impulse response and mutual radiation impedance between a circular piston and a piston of arbitrary shape,” *J. Acoust. Soc. Am.* **54**, 746–754 (1973).

³²P. R. Stepanishen, “Impulse response and radiation impedance of an annular piston,” *J. Acoust. Soc. Am.* **56**, 305–312 (1974).

³³P. R. Stepanishen, “Evaluation of mutual radiation impedances between circular pistons by impulse response and asymptotic methods,” *J. Sound Vib.* **59**, 221–235 (1978).

³⁴W. Thompson, Jr., “The computation of self- and mutual-radiation impedances for annular and elliptical pistons using Bouwkamp’s integral,” *J. Sound Vib.* **17**, 221–233 (1971).

³⁵W. Klippel and J. Schlechter, “Distributed mechanical parameters of loudspeakers, Part 1: Measurements,” *J. Audio Eng. Soc.* **57**, 500–511 (2009).

³⁶T. W. Leishman, “Active control of sound transmission through partitions composed of discretely controlled modules,” Ph.D. thesis, The Pennsylvania State University (2000), Chap. 7.

³⁷T. W. Leishman and J. Tichy, “An experimental investigation of two module configurations for use in active segmented partitions,” *J. Acoust. Soc. Am.* **118**, 1439–1451 (2005).

³⁸P. L. Gatti and V. Ferrari, *Applied Mechanical and Structural Vibrations: Theory, Methods, and Measuring Instrumentation* (E & FN Spon, London, 1999), p. 461.

³⁹P. Avitabile, “Modal space: What is the difference between all the mode indicator functions? What do they all do?,” *Exp. Tech.* **31**, 15–16 (2007).

⁴⁰M. H. Richardson, “Is it a mode shape, or an operating deflection shape?,” *Sound Vib.* **31**, 54–61 (1997).

⁴¹H. F. Olson, *Acoustical Engineering* (Professional Audio Journals, Philadelphia, 1991), Sec. 6.8.